Supplementary Material for:

"Using GNSS-based vegetation optical depth, tree sway motion, and eddy-covariance to examine evaporation of canopy-intercepted rainfall in a subalpine forest"

Sean P. Burns[1,2], Vincent Humphrey[3,4], Ethan D. Gutmann[2], Mark S. Raleigh[5], D. R. Bowling[6], and Peter D. Blanken[1]

[1]*Department of Geography, University of Colorado, Boulder, CO, U.S.A.*

[2]*NSF National Center for Atmospheric Research, Boulder, CO, U.S.A.*

[3]*Division of Geological and Planetary Sciences, California Institute of Technology, Pasadena, CA, U.S.A.*

[4]*Department of Geography, University of Zürich, Zürich, Switzerland*

[5]*College of Earth, Ocean, and Atmospheric Sciences, Oregon State University, Corvallis, OR, U.S.A.*

[6]*School of Biological Sciences, University of Utah, UT, U.S.A.*

1. **Supplemental Figures S1 to S16**

(a) gnssA Antenna on US–NR1 Tower

(b) gnssB Antenna (Taken from the Northwest)

Figure S1. Photos of **(a)** the gnssA antenna at the top of the US-NR1 26-m tower, and **(b)** the gnssB antenna mounted on a tripod above the forest floor. The white enclosure shown in **(b)**, housed the gnssB receiver and the photo is taken northwest of the antenna so that the trees south and southeast of the antenna are shown.

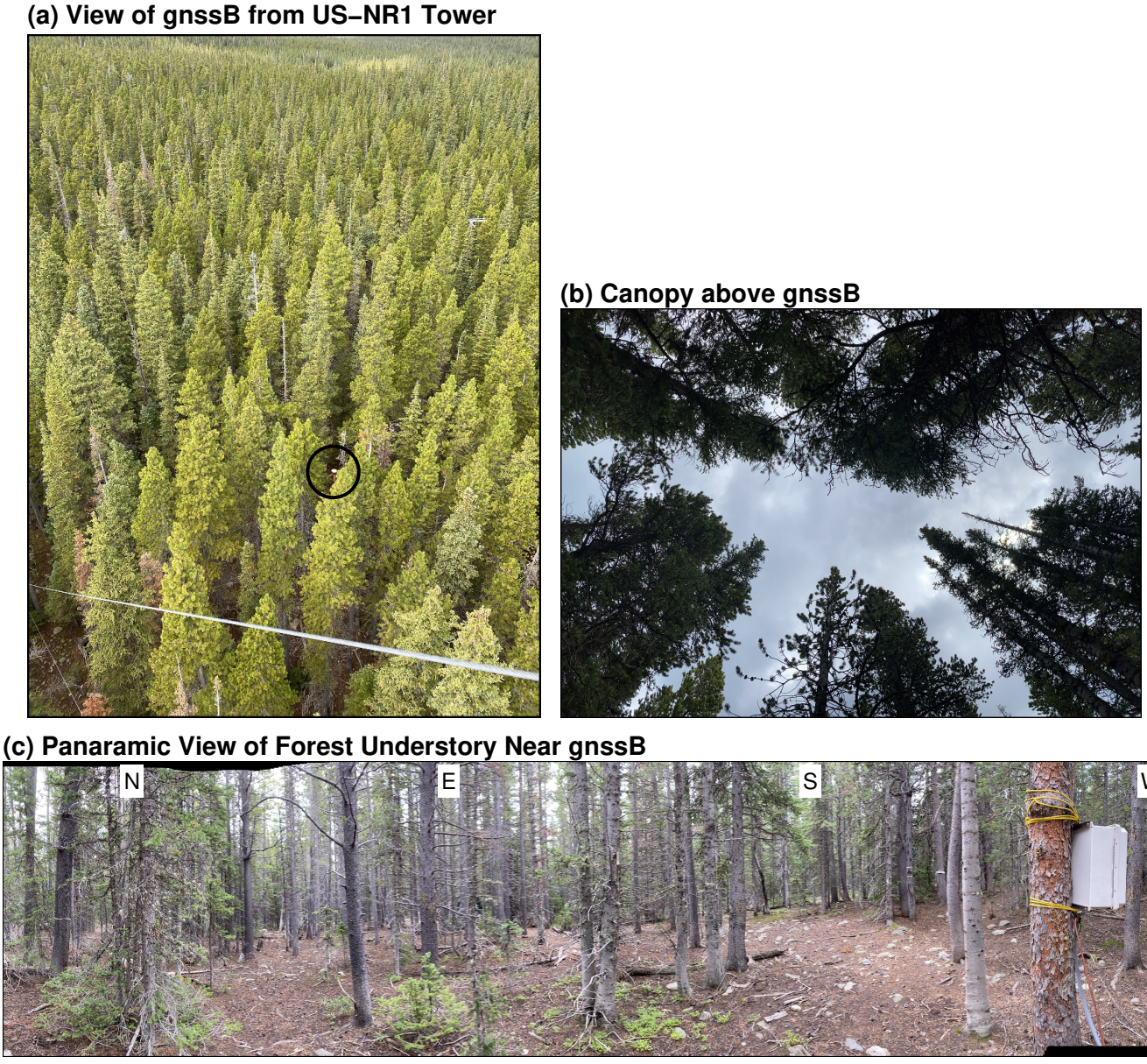

Figure S2. Photos of **(a)** gnssB taken from the top of the US-NR1 26-m tower (the gnssB antenna is visible as a white dot in the center of the black circle), **(b)** looking upward at the forest just-above the gnssB antenna, and **(c)** a panoramic photo of the understory looking at the swath of subcanopy that is south and east of the gnssB antenna.

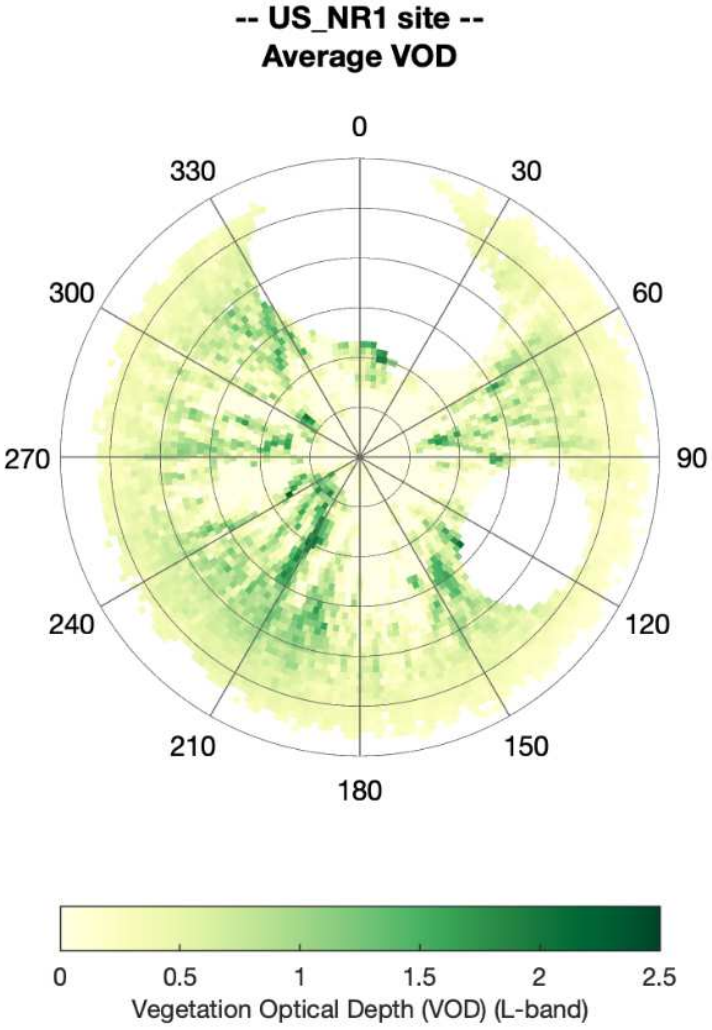

Figure S3. A skyplot of the mean VOD as a function of the radial direction from the subcanopy GNSS antenna. The white spaces show regions that were excluded from the VOD calculation due to the lightning dissipators at the top of the tower as well as fewer constellation tracks to the north.

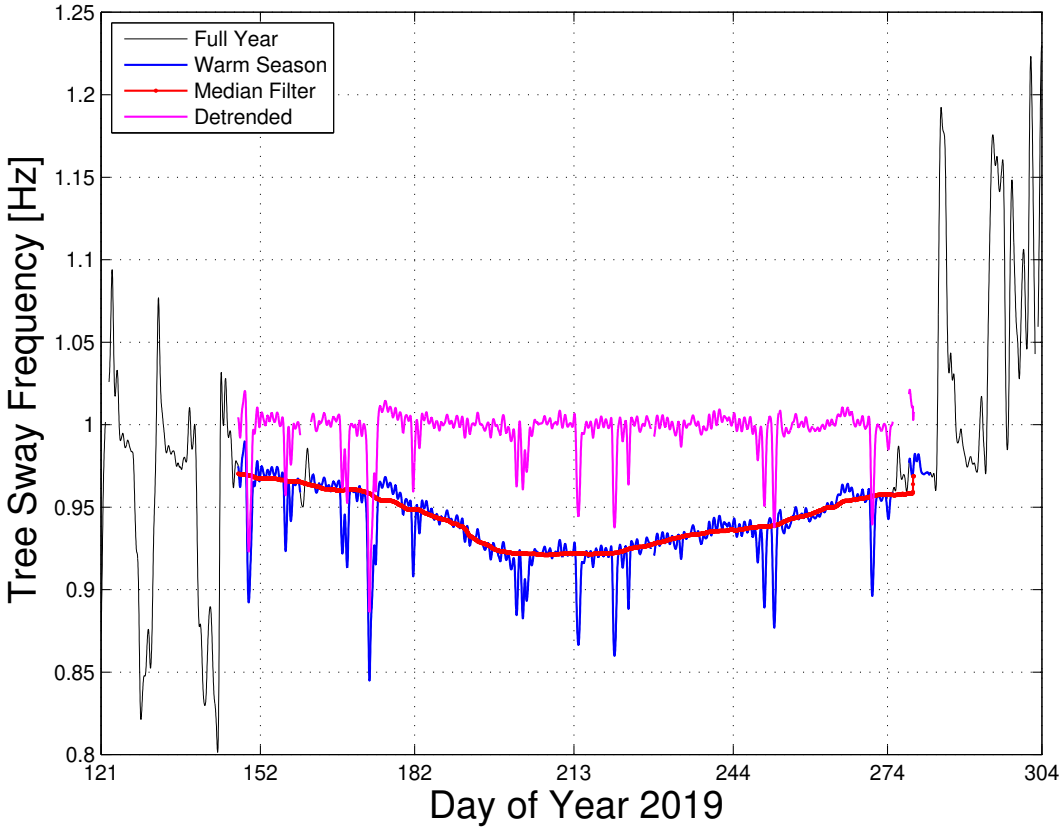

Figure S4. Time series of tree sway frequency for May-Oct of 2019. The 10-day sliding median filter (moving one 30-min sample at a time with the median centered on the 10-day mid-point) used to remove the low-frequency trend is shown along with the detrended tree sway frequency (see legend).

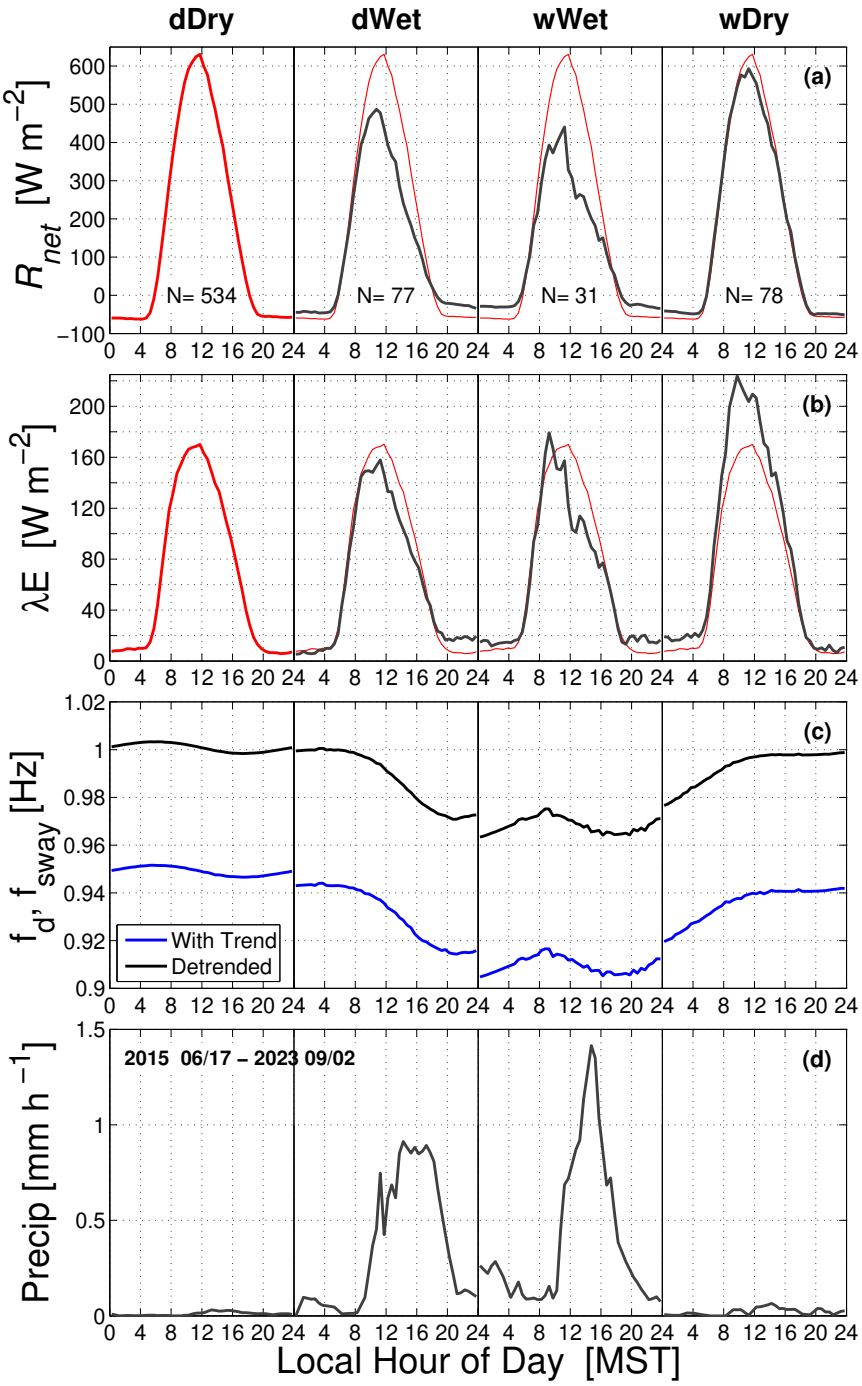

Figure S5. The composite diel cycle of **(a)** net radiation R_{net}, **(b)** latent heat flux λE, **(c)** tree sway, and **(d)** precipitation amount. In **(c)**, the diel cycle of tree sway for the raw data and with the low-frequency trend removed are both shown (see legend). These results are from the warm season between years 2015 and 2023, and the number of days (N) used for each diel cycle are shown in panel **(a)**.

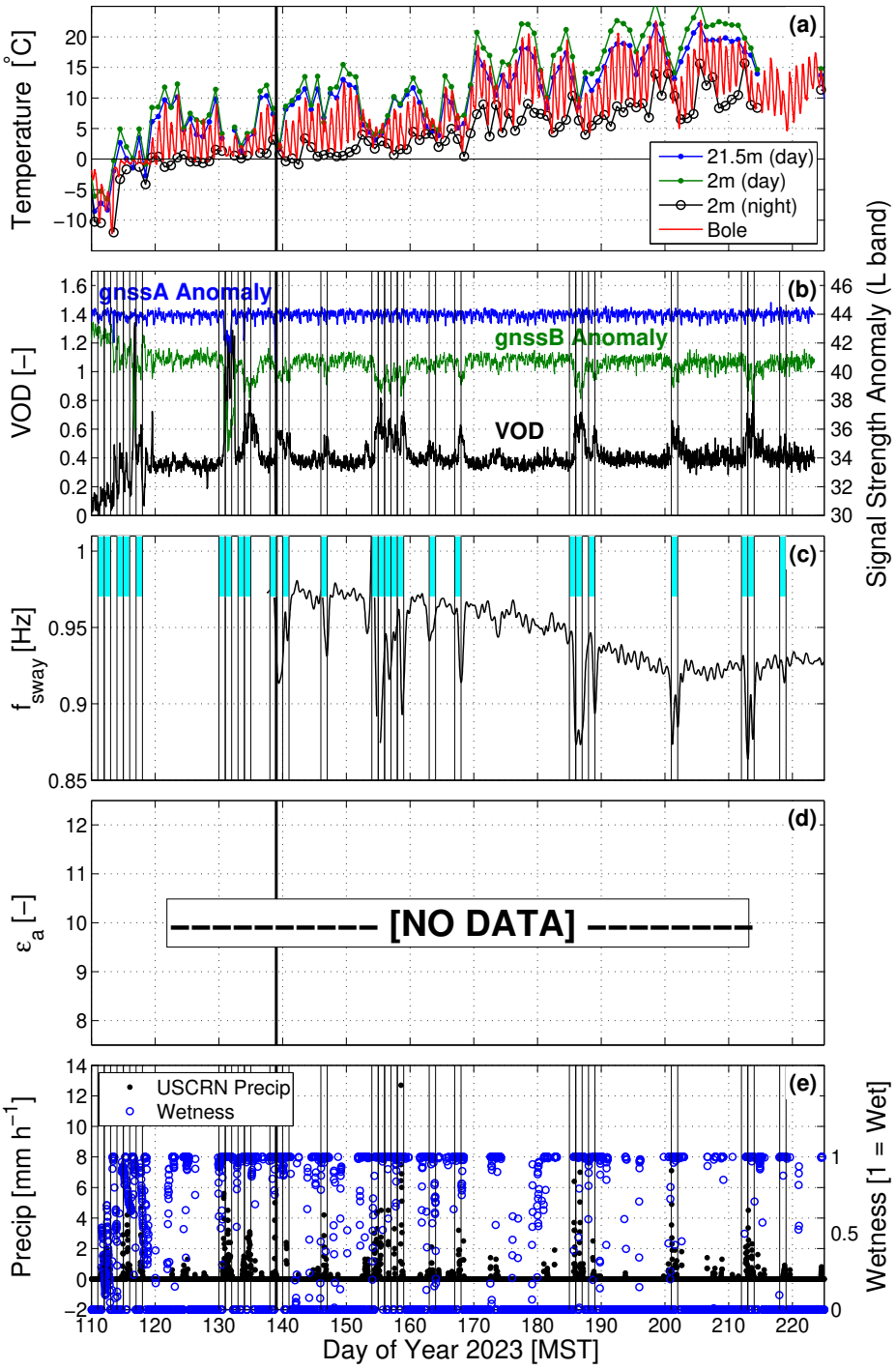

Figure S6. As in Fig. 2, but for the 2023 warm-season data.

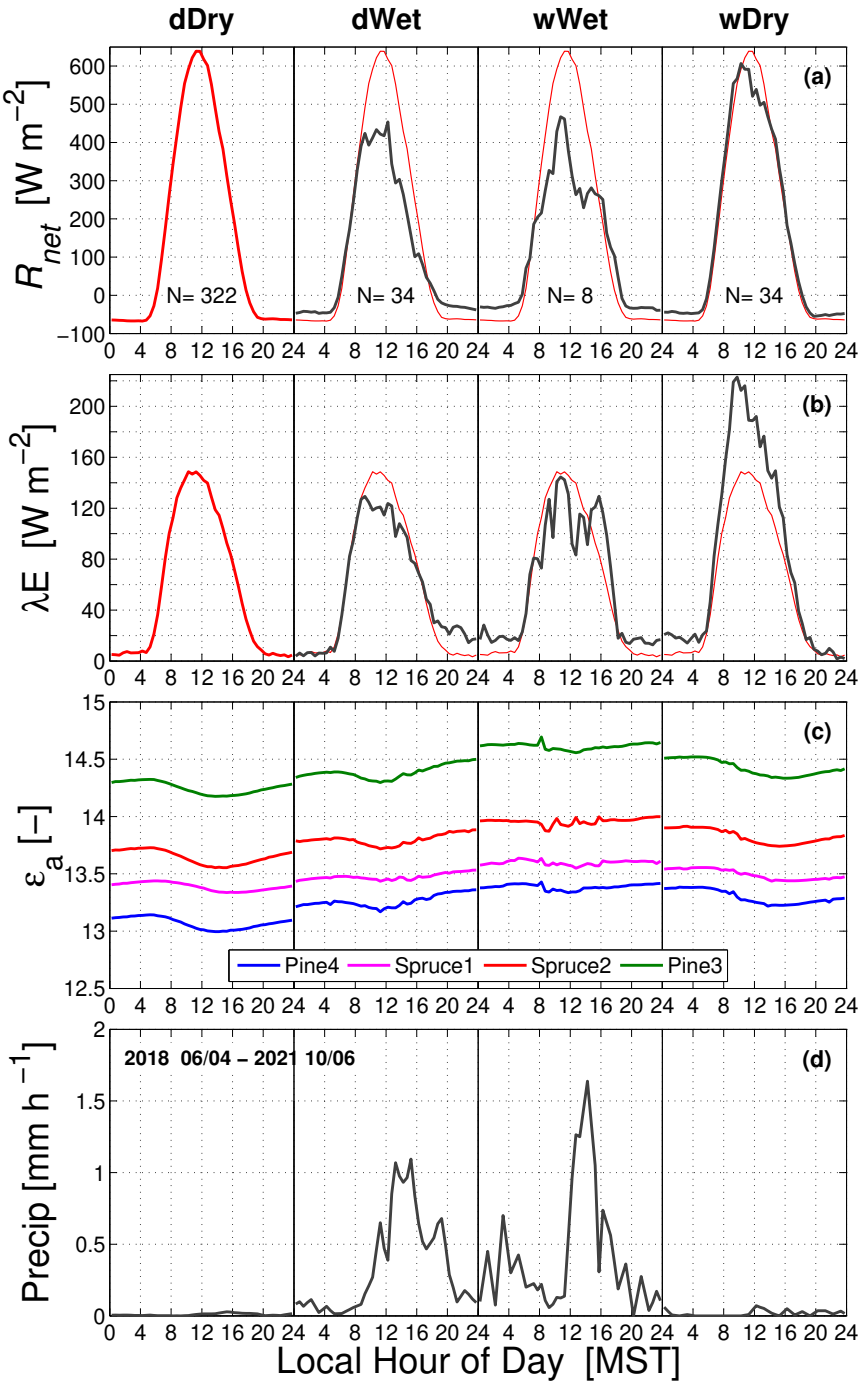

Figure S7. The composite diel cycle of **(a)** net radiation R_{net}, **(b)** latent heat flux λE, **(c)** dielectric permittivity ε_a from several GS3 sensors (see legend), and **(d)** precipitation. These results are from the warm season between years 2018 and 2021, and the number of days (N) used for each diel cycle are shown in panel **(a)**.

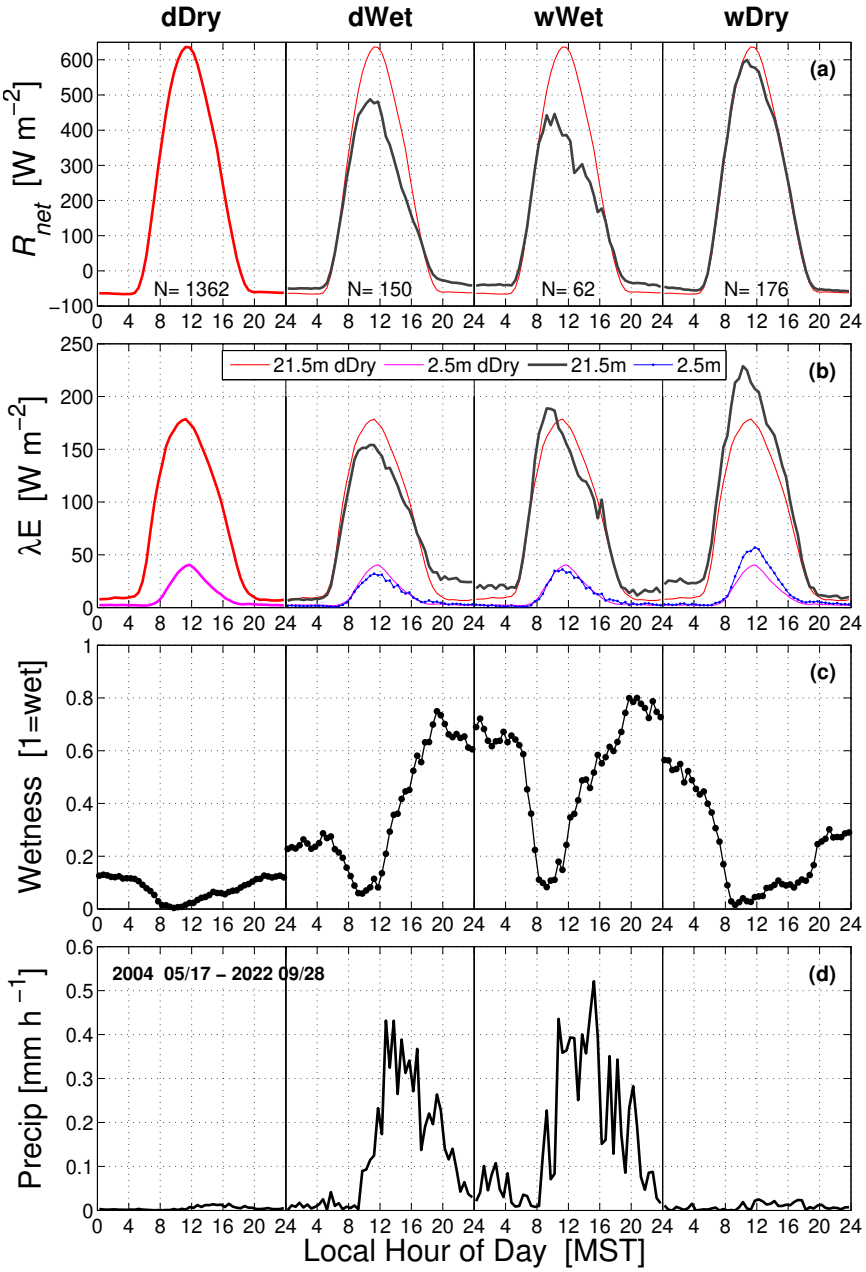

Figure S8. The composite diel cycle of **(a)** net radiation R_{net}, **(b)** latent heat flux λE, **(c)** wetness, and **(d)** precipitation. In **(b)**, both the above-canopy and subcanopy λE are shown (see legend). The wDry λE data are shown in Fig. 6a,b. These results are from the warm season between years 2004 and 2022, and the number of days (N) used for each diel cycle are shown in panel **(a)**.

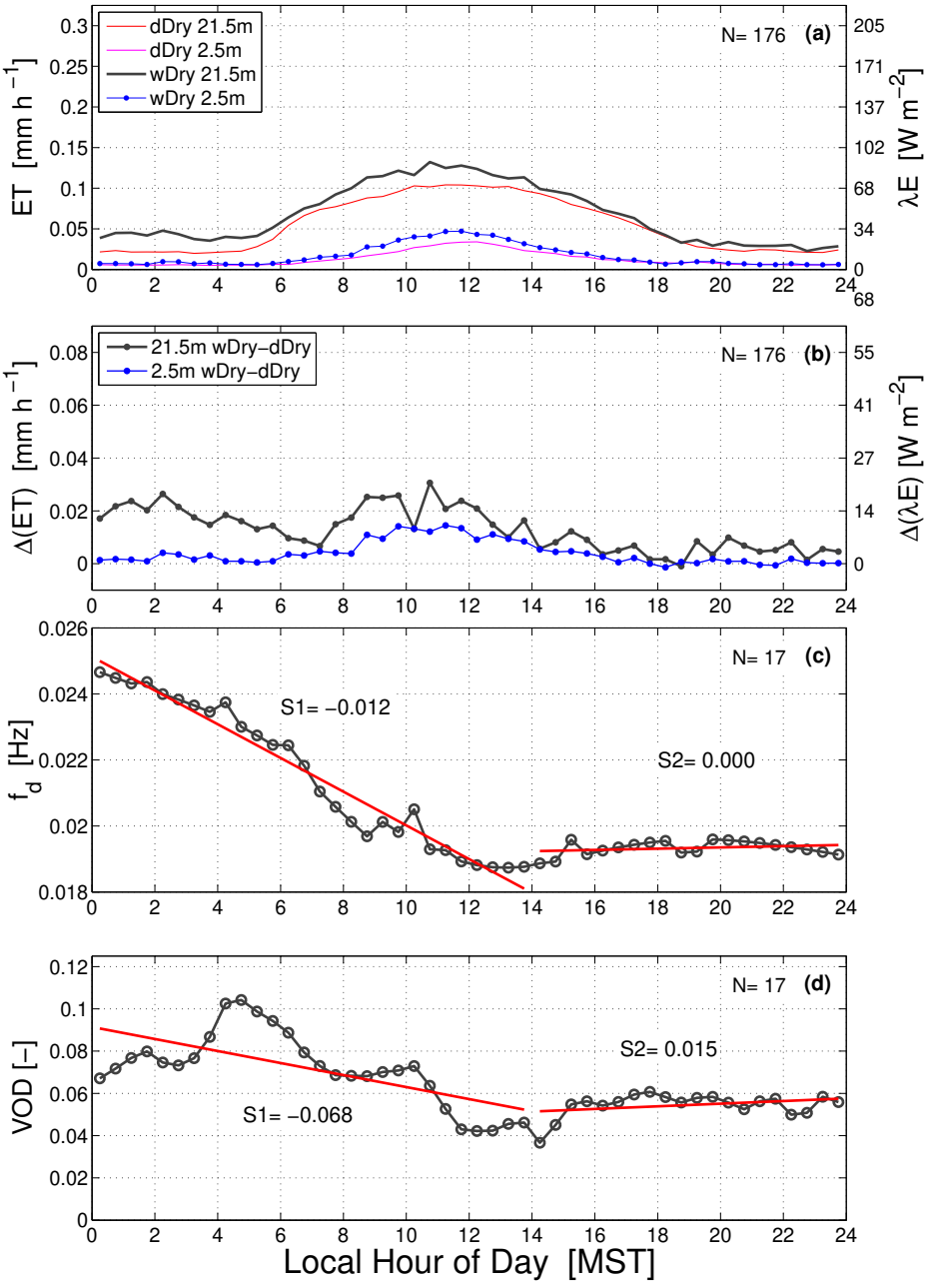

Figure S9. As in Fig. 6, but showing the standard deviation of the data within each time bin.

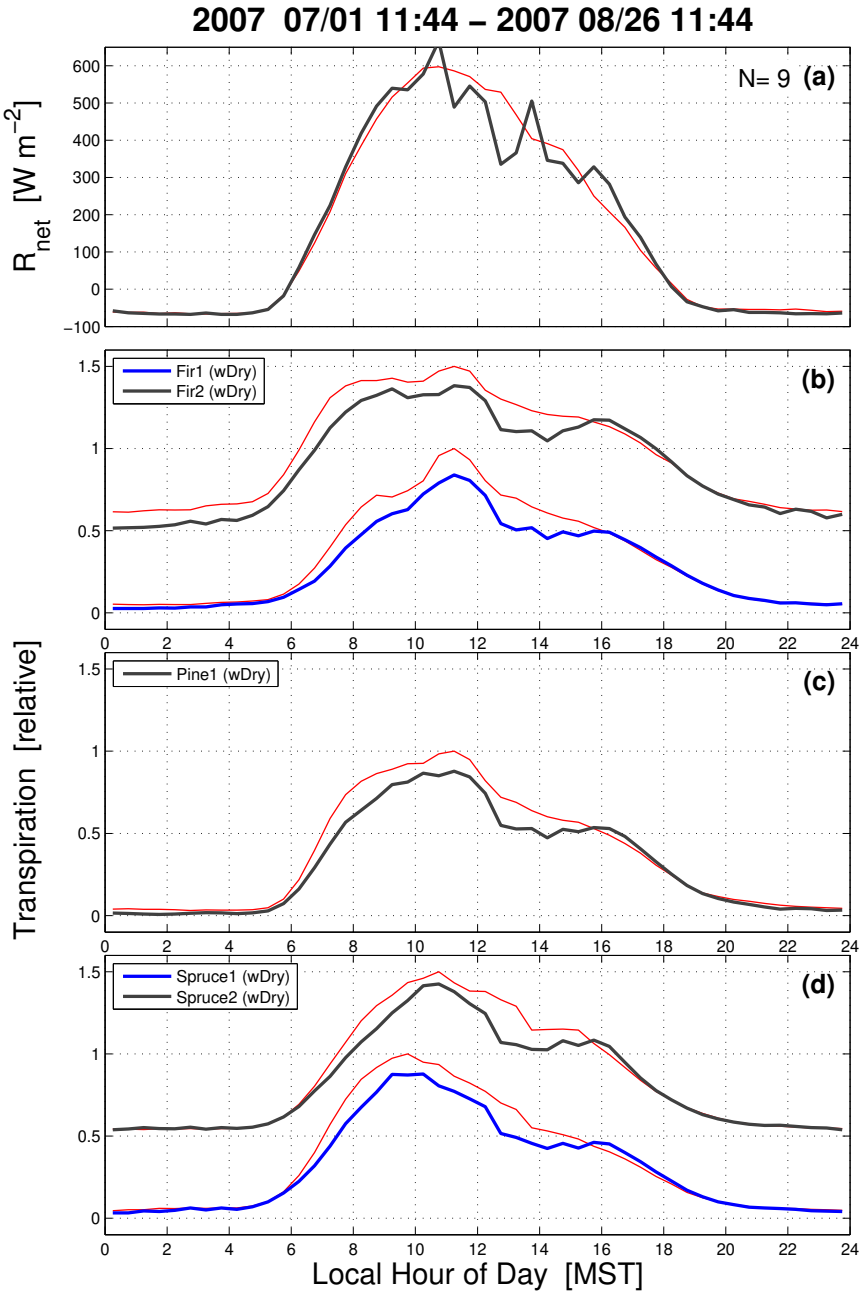

Figure S10. The mean 2007 warm-season composite diel cycle of **(a)** net radiation R_{net} and **(b)-(d)** normalized transpiration for five different trees (2 fir, 1 pine, and 2 spruce) from the sap flow measurements of Hu et al. (2010). The composite of dDry days are shown in red while the wDry days (N = 9 days) are in black or blue (see legend). When there are more than one tree, one of the diel cycles is offset by +0.5.

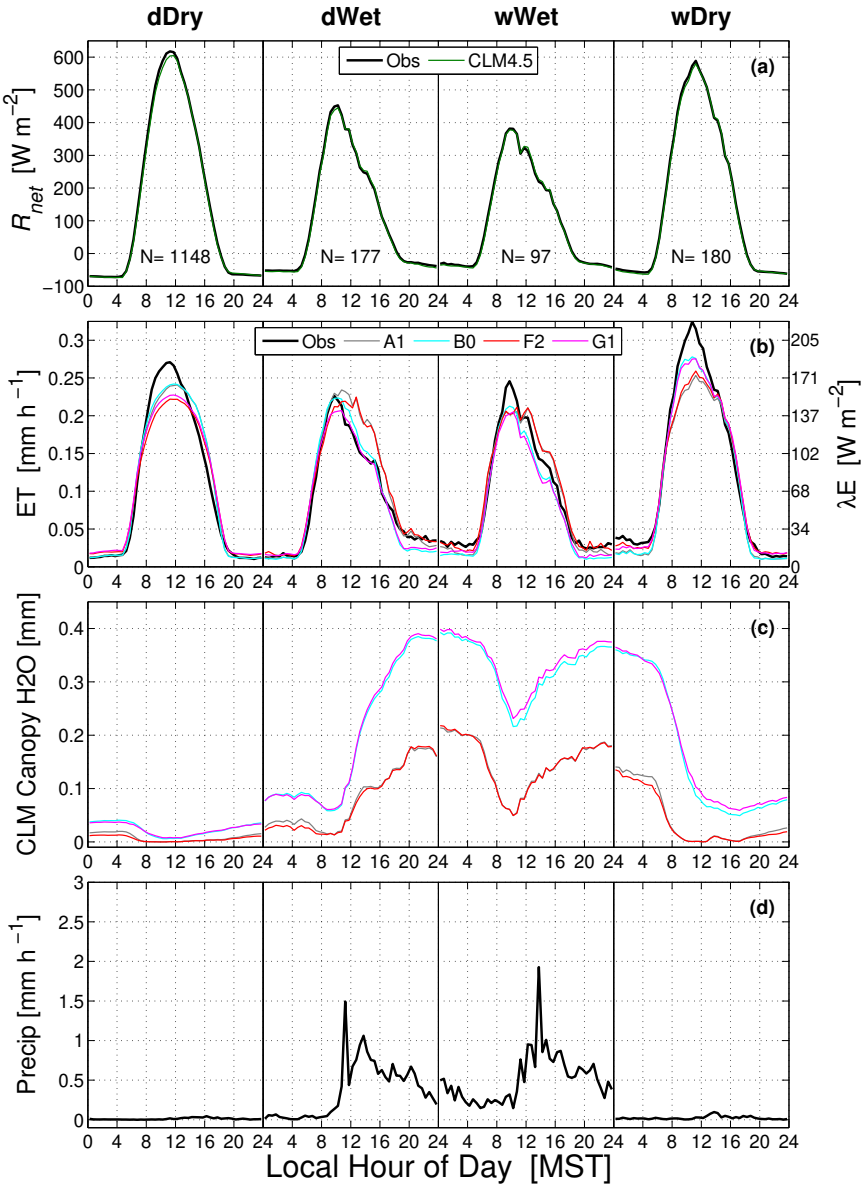

Figure S11. The warm-season mean composite diel cycle for dDry, dWet, wWet, and wDry conditions of **(a)** observed and CLM4.5 net radiation R_{net}, **(b)** observed and CLM4.5 evapotranspiration ET, **(c)** CLM4.5 canopy water content, and **(d)** precipitation. In **(b)** and **(c)** the CLM4.5 A1, B0, F2, and G1 cases are shown (see legend in panel **(b)** as well as Sect. 2.3 for case details). These results are from years 1999–2003 and 2006–2014 and are from the same periods used in Burns et al. (2018). The number of days (N) used for each diel cycle are shown in panel **(a)**.

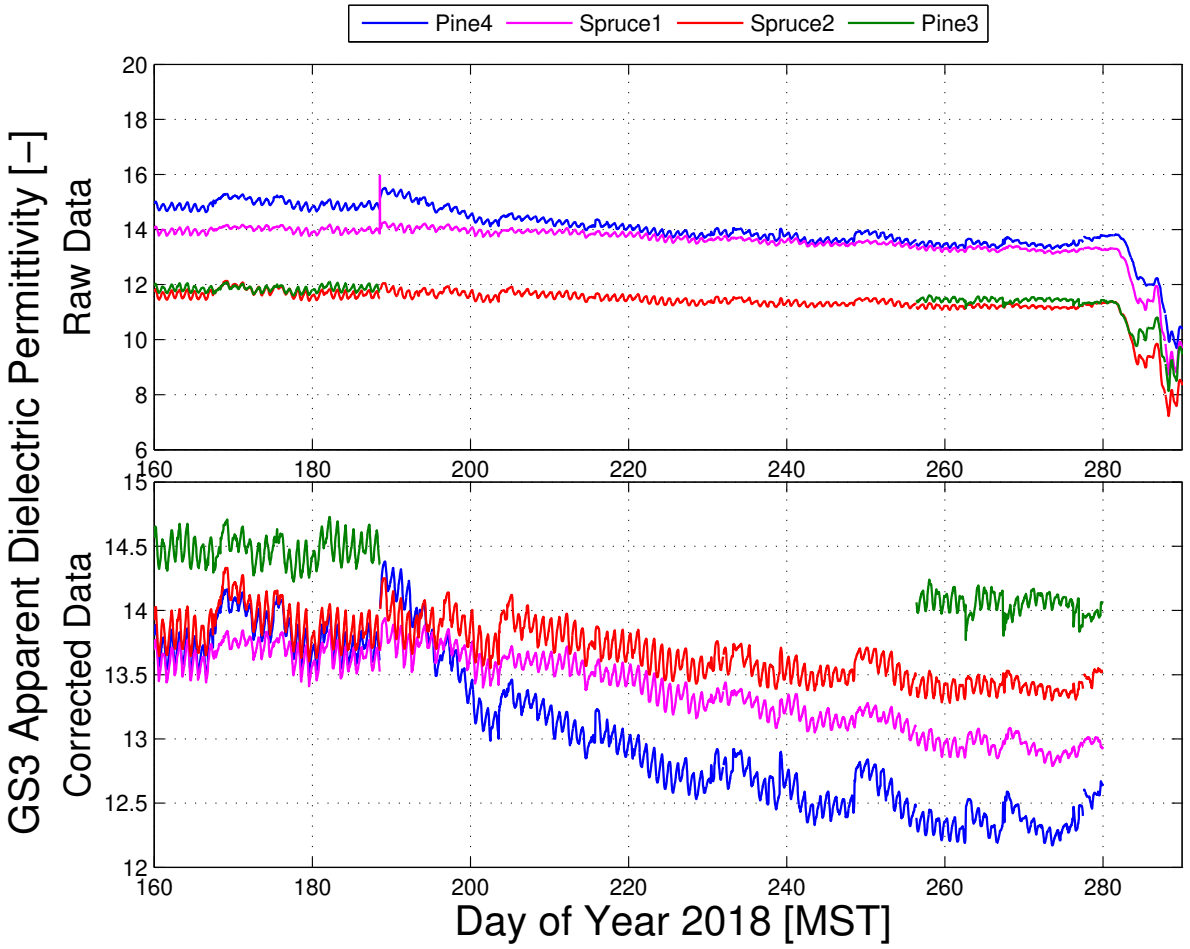

Figure S12. Time series of GS3 dielectric permittivity for the 2018 warm-season.

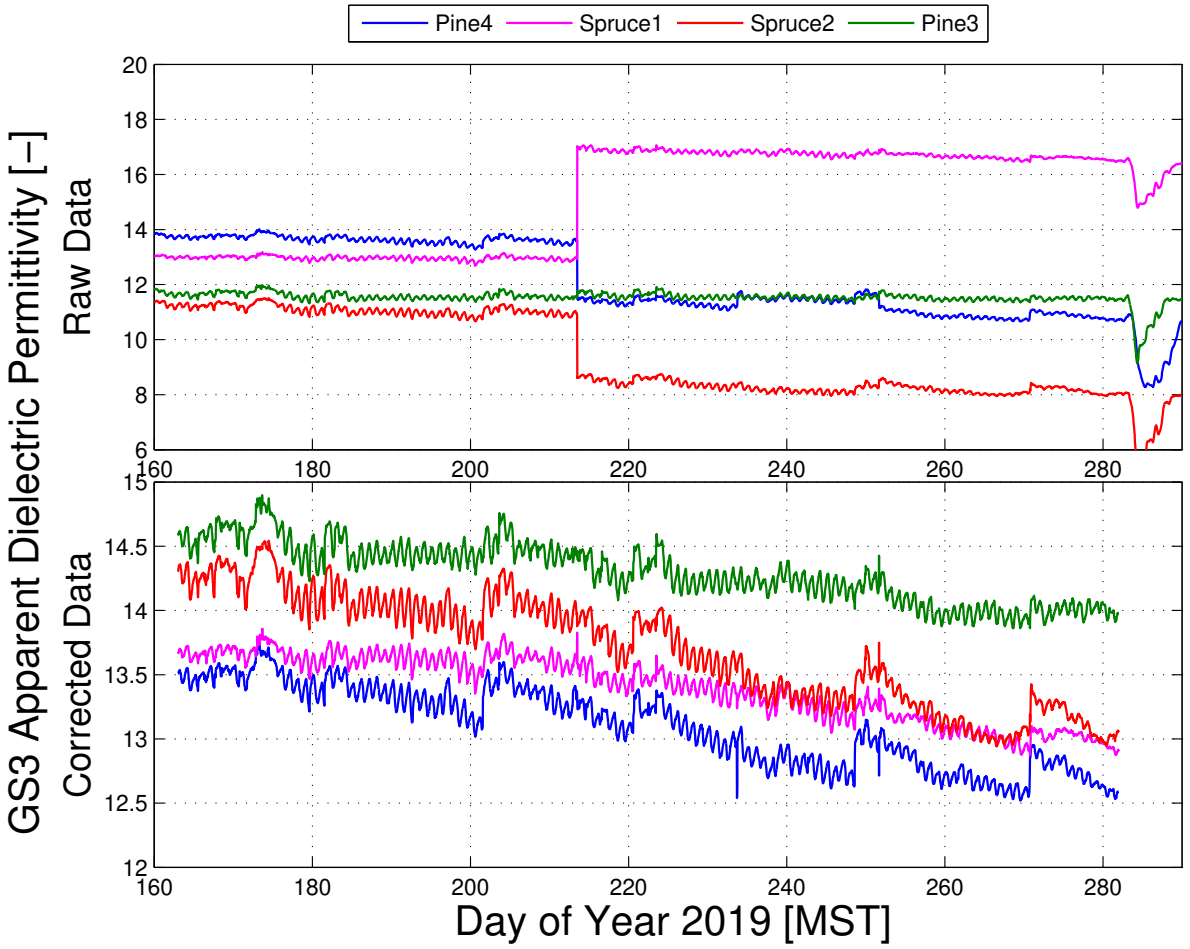

Figure S13. Time series of GS3 dielectric permittivity for the 2019 warm-season.

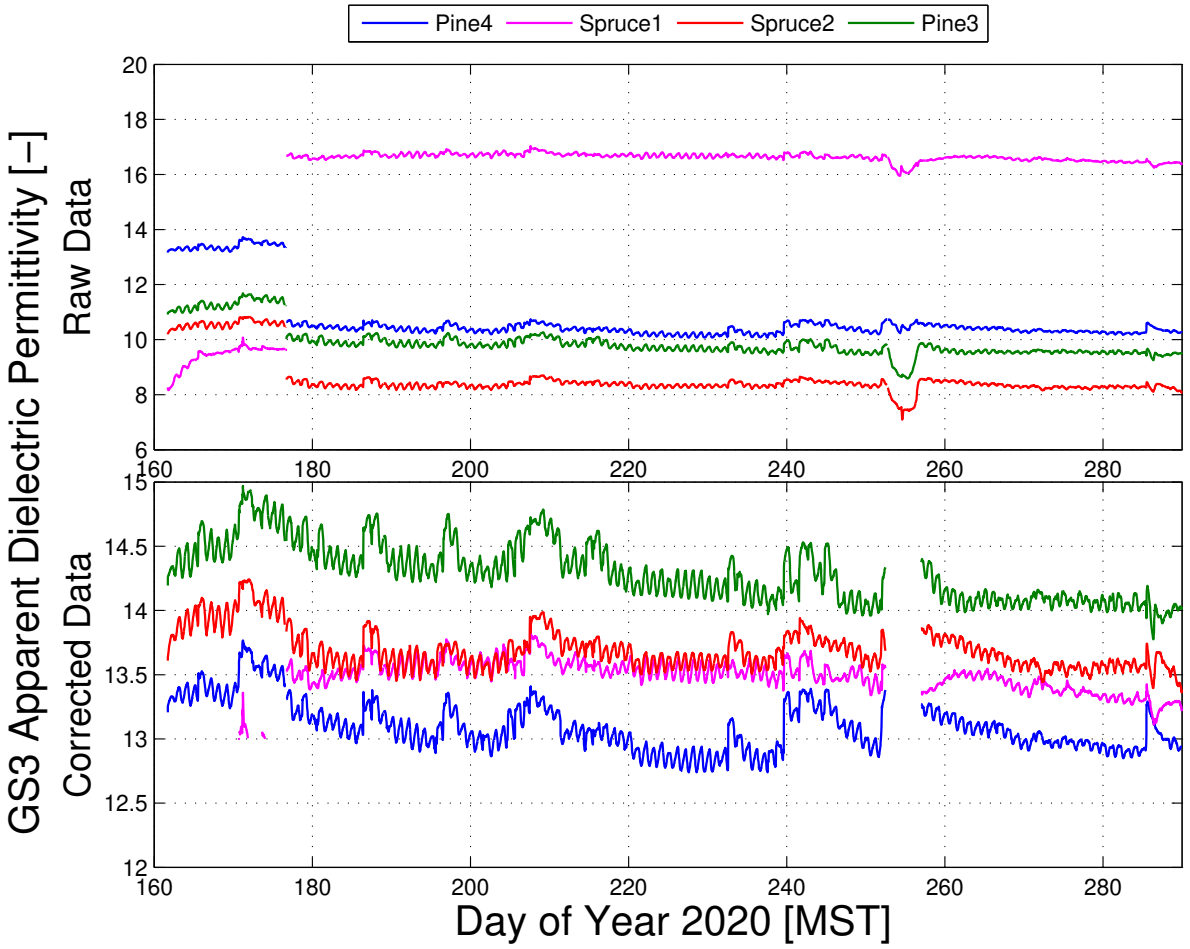

Figure S14. Time series of GS3 dielectric permittivity for the 2020 warm-season.

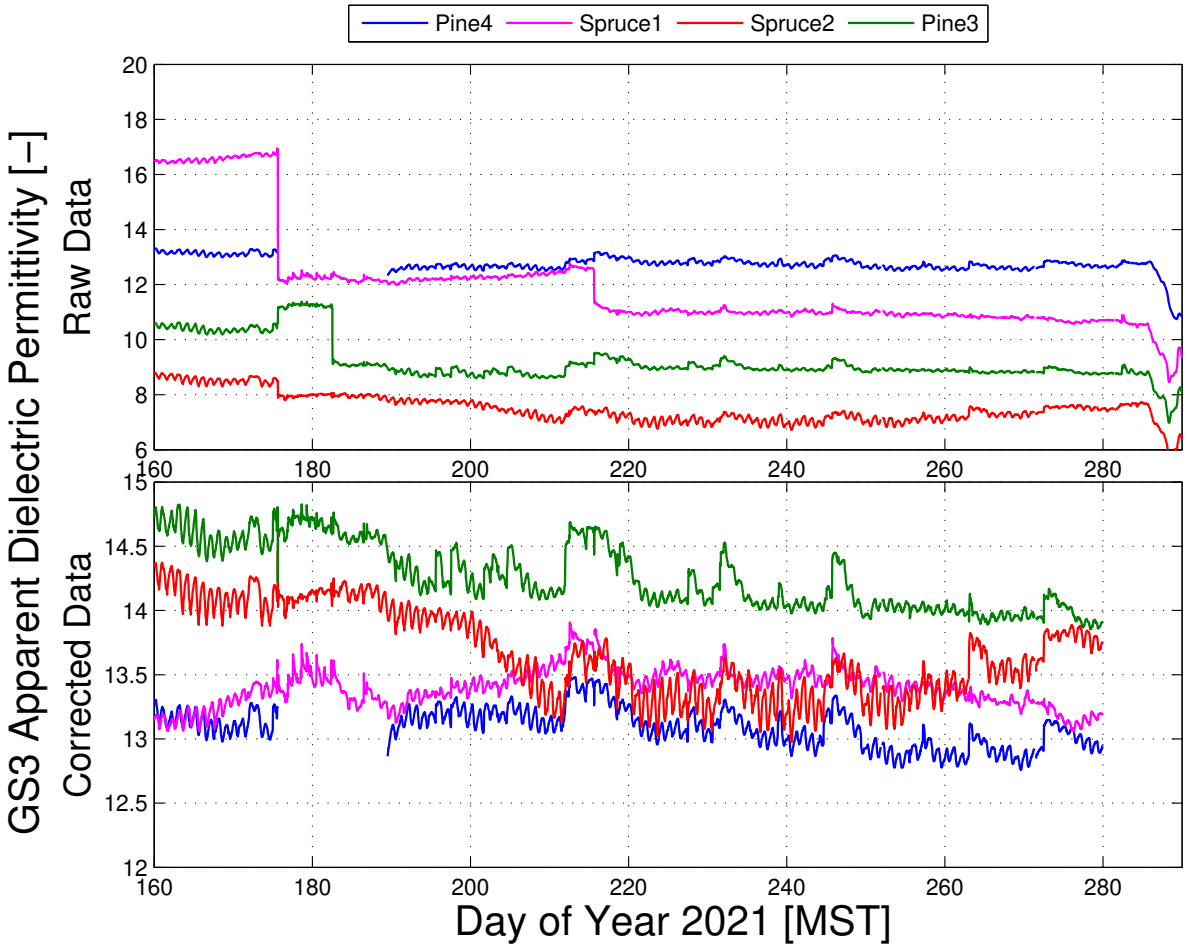

Figure S15. Time series of GS3 dielectric permittivity for the 2021 warm-season.

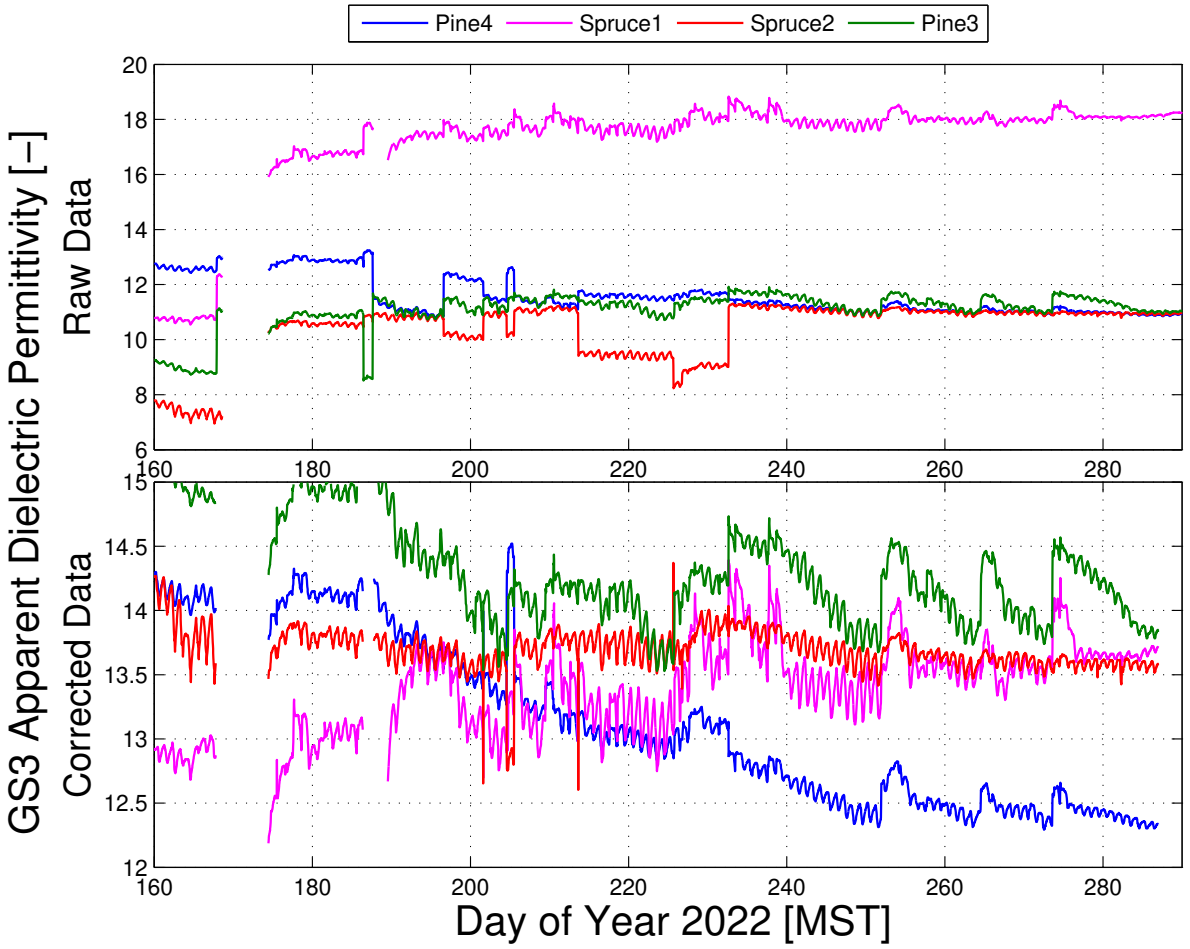

Figure S16. Time series of GS3 dielectric permittivity for the 2022 warm-season.